Quantified Pore-Scale Nanoparticle Transport in Porous Media and the Implications for Colloid Filtration Theory

Published In:
Langmuir

OPEN ACCESS

Quantified pore-scale nanoparticle transport in porous media and the implications for colloid filtration theory

Ian L. Molnar[1], Paula Sanematsu[2], Jason I. Gerhard[1], Clinton S. Willson[3] and Denis M. O'Carroll[1,4*]

[1]Department of Civil and Environmental Engineering, The University of Western Ontario, London, ON, Canada N6A 5B9

[2]Craft and Hawkins Department of Petroleum Engineering, Louisiana State University, Baton Rouge, LA 70803

[3]Department of Civil and Environmental Engineering, Louisiana State University, Baton Rouge, LA 70803

[4]School of Civil and Environmental Engineering, Connected Water Initiative, University of New South Wales, Manly Vale, NSW, 2093, Australia

*Corresponding author.

Denis M. O'Carroll: Tel +61 2 8071 9800

e-mail: docarroll@eng.uwo.ca

Abstract

This study evaluates the pore-scale distribution of silver nanoparticles during transport through a sandy porous medium via quantitative Synchrotron X-ray Computed MicroTomography (qSXCMT). The associated distribution of nanoparticle flow velocities and mass flow rates were obtained by coupling these images with Computational Fluid Dynamic (CFD) simulations. This allowed, for the first time, the comparison of nanoparticle mass flow with that assumed by the standard Colloid Filtration Theory (CFT) modelling approach. It was found that (i) 25% of the pore space was further from the grain than assumed by the CFT model; (ii) Average pore velocity agreed well between results of the coupled qSXCMT/CFD approach and the CFT model within the model fluid envelope, however, the former were 2 times larger

26 than the latter in the centers of the larger pores and individual velocities were upwards of 20

27 times those in the CFT model at identical distances from grain surfaces

28 ; and (iii) Approximately 30% of all nanoparticle mass and 38% of all nanoparticle mass flow

29 occurred further away from the grain surface than expected by the CFT model. This work

30 suggests that a significantly lower fraction of nanoparticles will contact a grain surface by

31 diffusion than expected by CFT models, likely contributing to inadequate CFT model

32 nanoparticle transport predictions.

Introduction

34   Predicting the transport of Engineered Nanoparticles (ENPs) through the subsurface is an

35 important and unresolved topic. ENPs are widely used in both industrial processes and consumer

36 products[1]; their prevalence suggests the likelihood of their presence in the subsurface and, if

37 mobile, may pose risks to municipal drinking water supplies or surface water bodies. Engineered

38 nanoparticles, such as nano-Zero-Valent-Iron (nZVI), are also being purposely injected into the

39 subsurface at contaminated industrial sites to degrade contaminants [2]. As a result, accurately

40 predicting the transport of ENPs through soil is valuable for both groundwater source zone

41 protection and designing efficient site-remediation schemes.

42   However, current modelling approaches cannot adequately simulate nanoparticle

43 transport through soil[3]. The classic approach to continuum-scale modelling of nanoparticle

44 transport employs the Advection-Dispersion Equation (ADE) with a first-order kinetic retention

45 coefficient (k_{att})[4] , which predicts a symmetric breakthrough concentration curve and a log-linear

46 concentration profile of retained nanoparticles[4]. However, nanoparticle transport experiments

47 generally exhibit non-symmetrical breakthrough curves with extended tailing behavior[5, 6, 7, 8, 9, 10]

48   and retention profiles that are either hyperexponential [5, 6, 11, 12, 13, 14, 15, 16, 17, 18, 19] or non-

49   monotonic [11, 12, 13, 14, 16, 17, 19, 20, 21, 22, 23]. The fundamental mechanisms driving these anomalous

50   nanoparticle transport behaviours have not yet been definitively identified as there is a poor

51   understanding of the pore-scale distribution and behavior of nanoparticles during transport in real

52   porous media [4]. This lack of pore-scale knowledge hinders the development of models that can

53   accurately describe, and predict, nanoparticle transport through soil.

54   The most common mechanistic model to predict k_{att}, Colloid Filtration Theory (CFT), has

55   been employed for a wide range of nanoparticles and environmental conditions[15, 24, 25, 26, 27, 28, 29,

56   30, 31, 32, 33, 34, 35]. CFT's mechanistic model employs a force/torque balance to calculate colloid

57   trajectories and attachment in the presence of a collector (or assemblage of collectors) to

58   determine the fraction of approaching colloids which contacts the collector surface: the 'contact

59   efficiency', η. The specific forces and torques, and boundary conditions, employed by each CFT

60   model is discussed in detail elsewhere [4]. The CFT-predicted η is then upscaled into the

61   continuum-scale k_{att} by applying a colloid mass balance over a continuum control volume filled

62   with identical collectors.

63   There are a number of different CFT mechanistic models that employ different

64   force/torque balances, environmental conditions and model geometries [36, 37, 38, 39, 40, 41]. A key

65   consideration is the Derjaguin-Landau-Verwey-Overbeek (DLVO) condition: favorable DLVO

66   conditions refer to scenarios with no repulsive energy barrier preventing attachment of the

67   colloid onto the grain. Under favorable DLVO conditions, CFT mechanistic models generally

68   well describe micron-sized colloid retention[4], but over-predict nanoparticle retention [8, 38]. It

69   should be noted that this over-prediction is different from the phenomenon of CFT models

70   predicting η values greater than 1 at very low fluid velocities, which a number of recent studies

71   have attempted to address [38, 42, 43]. The over-prediction of nanoparticle attachment discussed in

72   this study is an over-prediction relative to experimental observations which appears even in the

73   CFT models and correlation equations that have been specifically modified to prevent η values

74   greater than $1^{[38]}$. For unfavorable DLVO conditions, CFT models are unable to predict

75   experimental retention rates for micron or nano-sized particles[44] due to the presence of a

76   repulsive DLVO energy barrier which prevents direct attachment of the colloid onto the collector

77   surface. The most common approach to adapting CFT for use in unfavorable conditions is to fit

78   k_{att} to experimental results via an additional parameter: α, 'attachment efficiency'. The α

79   parameter acts as a multiplier for η (which was derived assuming favorable conditions) to

80   describe the fraction of nanoparticles contacting a collector surface that remain attached to the

81   surface in unfavorable conditions. This modified '$\alpha\eta$' parameter is adjusted until the model

82   result matches up with the experimental observations. However, by employing α as a multiplier

83   for η, studies that attempt to predict α or examine the influence of parameters on α are limited by

84   the implicit assumption that CFT is able to accurately predict η.

85   It has been hypothesized that CFT's over-prediction of η relative to experimental

86   observations for nanoparticles is due, in part, to the mechanistic models' assumptions about pore

87   and grain geometry[8, 45, 46]. The typically assumed geometry is a perfectly spherical collector (i.e.,

88   grain) surrounded by a shell of fluid – termed the Happel Sphere-In-Cell (HSIC) [37, 38, 40, 47, 48].

89   Recently, Molnar et al. [49] developed a quantitative-Synchrotron X-ray Computed

90   MicroTomography technique (qSXCMT) to determine the pore-scale concentration distribution

91   of nanoparticles in soil columns during transport experiments. The qSXCMT method was then

92   used by Molnar et al. [8] to illustrate how CFT's over-prediction of η for nanoparticles could be

93   linked to regions of relatively low fluid velocity near grain-grain contacts, a feature not

94   accounted for within the HSIC geometry. The study also linked these low velocity regions to the

95   extended tailing behavior often observed in nanoparticle experiments [8].

96   However, other simplifying assumptions within the HSIC geometry may be further

97   preventing CFT models from accurately predicting nanoparticle transport. For one, it assumes

98   the average flow field through a realistic porous medium can be approximated by the analytical

99   solution of creeping flow through the Happel fluid envelope. As well, it approximates the pore-

100   space as a narrow shell of fluid through which all nanoparticles flow. A number of studies have

101   indicated that realistic flow fields may not be consistent with CFT[8, 50, 51, 52]. However, these pore-

102   scale assumptions, fundamental to the HSIC geometry and thus CFT predictions, have never had

103   their validity tested for actual nanoparticle transport through real porous media.

104   In this study, qSXCMT and Computational Fluid Dynamics (CFD) are employed to

105   determine, for the first time, the averaged distribution of nanoparticle mass *flux* (mass flow per

106   unit area, italicized to avoid confusion with mass flow) and flow rates within a soil's pore spaces.

107   qSXCMT was coupled with CFD to characterize the averaged pore-scale nanoparticle

108   distribution and flow field during a nanoparticle column transport experiment. A silver

109   nanoparticle solution was injected into a column packed with uniform quartz sand under

110   unfavorable DLVO conditions and was imaged via qSXCMT at regular intervals during

111   nanoparticle injection and elution. First, this study computationally characterized the distribution

112   of pore space within the soil and examined how well experimentally determined, bulk-measured

113   lab properties (i.e., soil sieve analysis) described the imaged pore and grain geometry. Then, the

114   distribution of fluid velocity through the soil was estimated via CFD simulations and compared

115   to analytical solutions for creeping flow in the HSIC geometry. Next, the distribution of

116   nanoparticle mass within the pore space was determined by qSXCMT and coupled with the

117 CFD-simulated velocity distribution to estimate silver nanoparticle mass *flux* and mass flow rate

118 distributions. The findings provide some of the first experimental insights into how pore-scale

119 nanoparticle behaviour impacts continuum-scale transport as well as yielding significant insight

120 into why predicting nanoparticle transport remains a challenge for CFT.

121

Materials and Methods

123 A silver nanoparticle (nAg) transport experiment was undertaken at the GeoSoilEnviro

124 Center of Advanced Radiation Sources (GSECARS) 13-BM-D beamline at the Advanced Photon

125 Source, Argonnne National Lab. The experimental method is described in detail in Molnar et al.

126 [8]; a summary of the relevant details are provided here. Note that the nAg transport experiment

127 and corresponding SXCMT datasets examined here were also used in Molnar et al. [8], there

128 described as the 'Uniform Quartz' dataset. The analysis presented here is entirely new; this paper

129 does not re-use or re-present any results from the Molnar et al. [8] study.

Materials

131 Silver nanoparticles were synthesized by reducing silver nitrate (0.1N, Alfa Aesar) with

132 sodium borohydride (Granulated, 97+%, Alfa Aesar) and electrosterically stabilized with a 1%

133 solution of carboxymethylcellulose 90k (CMC90k). The synthesis procedure is discussed in

134 detail elsewhere [8, 49]. CMC90k is a polymer that is typically employed to stabilize bi-metallic

135 particles (i.e. nZVI) for site remediation due to its superior stabilization[2, 53, 54]. Previous studies

136 have employed CMC90k as an nAg stabilizer and discuss its nAg-stabilization properties in

137 greater detail [8, 49]. It has been shown that CMC90k does not compete with nAg for deposition

138   sites and does not alter nAg deposition rates onto the quartz surface [8]. The synthesis procedure

139   occurred at the GSECARS wet lab the day before the allotted synchrotron beam time. The

140   synthesized silver nanoparticles were analyzed via Dynamic Light Scattering and were found to

141   have an average hydrodynamic diameter (d_{50}) of 29.8 nm and a zeta potential of -27.97 mV. The

142   viscosity of the final CMC90k stabilized solution was 14 cP. An additional solution of silver

143   nanoparticles was synthesized using an identical method for the purpose of TEM imaging.

144   Approximately 24 hours elapsed between the second solution synthesis and creating the TEM

145   grids to be consistent with the time between initial synthesis and qSXCMT imaging. The

146   resulting TEM image is presented in Molnar et al [8]. A size analysis of the particles within the

147   TEM image was conducted using ImageJ which identified 85 nanoparticles with an average

148   diameter of 13.8 nm (maximum: 61.9 nm, minimum: 1.6 nm) and a standard deviation of 12.3

149   nm.

150   The porous medium employed for the transport experiment was a quartz sand (Unimin

151   Accusand) that had been cleaned by rinsing with Nitric Acid (Environmental grade, Alfa Aesar)

152   followed by rinsing with deionized water and left to dry overnight. The sand was sieved to

153   achieve a specific grain size distribution (420 – 600 µm) and was then wet-packed into a small

154   aluminum column (ID: 5.6 mm, length: 5 cm). Rigorous packing procedures (which included

155   stirring, vibrating and tamping) were undertaken to ensure that the column was uniformly packed

156   throughout and to avoid edge effects throughout the column. The solution used for wet packing

157   contained no nanoparticles but was controlled to the same viscosity (i.e. 1% CMC90k solution at

158   14 cP) and ionic strength (120 mM, achieved with Sodium Nitrate) as the nAg solution. The

159   porosity of the column (33%) was determined by measuring the specific gravity of the sand (2.65

160   g/cm^3) and weighing the amount of sand packed into the column.

161   Standard DLVO theory was used to estimate the DLVO energy profile for the uniform

162   quartz sand and is described in detail in Molnar et al.[8]. Briefly, the zeta potential for the quartz

163   sand was taken from literature values to be -55 mV[12] as it was found to have little impact on the

164   DLVO profile. The calculated DLVO profile, presented in Molnar et al [8], indicated that the

165   quartz sand was unfavorable to silver nanoparticle attachment in the experimental conditions and

166   contained a small repulsive energy barrier with a magnitude of 8.5 kT.

Silver nanoparticle transport experiment

168   The packed column was loaded into the imaging hutch and a pre-injection image was

169   collected. Following pre-injection imaging, the silver nanoparticle solution was injected with a

170   syringe pump at 0.11 mL/min. The flow direction was upwards through the column. A total of 3

171   pore volumes (PV's) of nAg solution was injected into the column and qSXCMT imaging

172   occurred at 0.25, 0.5, 0.75, 1 and 2 PV's of injection. The column was imaged at its midpoint,

173   2.55 cm above the base of the porous medium. The length of column section imaged (referred to

174   as the 'SXCMT imaging window') was 0.51 cm and extended from 2.55 cm to 3.06 cm above

175   the base of the column. The concentration of silver nanoparticles in the injection solution was

176   measured at the beginning and end of the nAg injection period via acid-digestion and ICP-OES

177   analysis. The average silver nanoparticle concentration being injected into the column was

178   determined to be 2.48 g/L (+/- 0.06 g/L).

179   After injecting 3 PV's of the nAg solution, the input was switched to a 1% CMC90k

180   solution with no silver nanoparticles – controlled to the same pH and ionic strength as the wet

181   packing and nAg solutions – to flush the nanoparticles out of the column. The column was

182   imaged after 1 and 2 PV's of elution and elution continued for an additional 5 PV's (7 PV's of

183 elution total) with no additional qSXCMT imaging. During injection and elution, samples were

184 collected from the column's effluent and analyzed for total silver concentration via ICP-OES

185 and, following the experiment the sand was acid-digested to test for retained nanoparticle

186 concentration. The results from the effluent sampling and acid-digestion are presented elsewhere

187 [8].

188 It should be noted that the results of this study are presented in terms of SXCMT pore

189 volumes (SXCMT-PV's) injected, not total column pore volumes. An SXCMT-PV is defined as

190 the pore space between the bottom of the column and the center of the imaging window

191 (approximately 0.22 mL) whereas a total column pore volume (PV's) refers to the pore volume

192 of the entire column (approximately 0.4 mL). Thus '1 SXCMT-PV's injected' refers to when the

193 advective front of the injected nAg solution reaches the center of the SXCMT imaging window.

194 qSXCMT imaging occurred at 0.4, 0.9, 1.3, 1.8, 3.6, 7.2 and 8.9 SXCMT-PV's corresponding to

195 0.25, 0.5, 0.75, 1, 2, 4 and 5 total column pore volumes. Incorporating these separate definitions

196 of pore volumes allows for a comparison of the relative position of the advective front of the

197 injected nAg solution to the SXCMT imaging window and the column's effluent.

198 **SXCMT imaging, reconstruction and analysis**

199 The specific imaging procedure required for qSXCMT imaging of silver nanoparticles in

200 a porous medium is discussed in detail elsewhere [8, 49]. Briefly, during qSXCMT imaging all flow

201 through the column was stopped, approximately 40 min/dataset; this stoppage time has no impact

202 on pore-scale nAg distribution[8].The column was then imaged four times in a single location to

203 collect four datasets of linear mass attenuation values at different x-ray energies above and below

204 the silver K-edge of 25.514 keV. The voxel resolution of the collected images was determined to

205   be 9.87 μm/voxel. Image reconstruction produced a 3-dimensional dataset of x-ray linear mass

206   attenuation values averaged over a 9.87×9.87×9.87 μm^3 voxel.

207   Sub-volumes of 350×350×450 voxels were cropped from the reconstructed datasets at

208   each time-step (40 minute imaging period) to remove edge effects and column material and

209   underwent a segmentation into water and solid using an indicator kriging technique [55, 56]. Grain

210   characteristics and pore-network structure within each segmented image were then extracted and

211   characterized using the method of Thompson et al. [57, 58]. This method assigns a unique identifier

212   to every pore and grain within the segmented sub-volumes as well as topological properties. The

213   three-dimensional segmented sub-volume of the pre-injection dataset, as well as a two-

214   dimensional slice of raw reconstructed gray values, are presented in Figure S1 (supplementary

215   information) to illustrate the structure of the porous medium within the SXCMT imaging

216   window. In addition, an algorithm was employed for each imaged time-step to measure the

217   distance between each pore space voxel and the closest grain surface voxel (see supplementary

218   information).

Quantifying silver nanoparticle concentrations within the SXCMT sub-volumes

219
220

221   The method of Molnar et al. [49] was employed to calculate the qSXCMT-determined silver

222   nanoparticle concentration for each pore-space voxel in the cropped sub-volume for the above-

223   mentioned time-steps. Briefly, for each time-step the below-edge dataset (25.414 keV) was

224   subtracted from each of the 3 above-edge datasets (25.614, 25.714, 25.814 keV) to create 3

225   difference datasets. Then, using the solid/pore segmented datasets created earlier, a modified

226   form of the Beer-Lambert law [49] was applied to every single pore-space voxel in all 3 difference

227   datasets to create 3 unique 'SXCMT-determined concentration' datasets for silver nanoparticles.

228   The 3 datasets were averaged together to create 1 final SXCMT-determined nanoparticle

229   concentration dataset for each imaged time-step. Each of the qSXCMT-determined datasets

230   (corresponding to each imaged time-step) were calibrated using a previously created calibration

231   procedure described in Molnar et al. [8]. This qSXCMT procedure does not accurately determine

232   nanoparticle concentration on a voxel-by-voxel basis due to noise associated with qSXCMT

233   imaging. However, averaging the approximately 16 million voxels with various techniques can

234   accurately quantify average spatial and temporal changes in nanoparticle concentrations within

235   the bulk pore space at a resolution similar to the imaged resolution (10.47 μm/voxel)[8, 49].

236   Moreover, this qSXCMT method is currently unable to accurately determine nanoparticle

237   concentrations within 17.3 μm of the grain surface due to a 'shadow zone' effect caused by x-ray

238   refraction at the grain/pore interface (this width is experiment specific and should not be taken as

239   a general value) [49]. Thus, all pore-space voxels within the 'shadow zone' in each qSXCMT-

240   determined concentration dataset are discarded during this quantification and calibration process.

Fluid Dynamics Modeling within the Image-derived Pore Space

242   Computational Fluid Dynamics (CFD) modeling was employed to simulate fluid flow in

243   a uniform quartz SXCMT dataset (referred to hereafter as the 'image-derived pore space' to

244   avoid confusion with the qSXCMT datasets, see Figure S1). A single dataset was employed for

245   CFD modeling (0 PV, i.e. pre-injection) as it can be assumed that the flow field did not change

246   throughout the injection or elution period because the extracted pore network statistics were

247   similar for all datasets.

248   First, unstructured tetrahedral meshes were generated using an in-house code[59, 60]. In

249   order to assess if the simulated fluid flow was sensitive to mesh resolution, meshes of increasing

250 resolution were generated for a smaller domain (150✕150✕350 voxels) until flow rate and

251 velocity profiles converged (i.e., no longer changed). Then, a resolution within the converged

252 range that was also computationally feasible for the large domain (350✕350✕450 voxels) was

253 used for the final mesh.

254   CFD modeling was conducted using an in-house three-dimensional Finite Element

255 Method (FEM) algorithm [60, 61] which solves the Stokes equation on the unstructured mesh.

256 Constant traction (normal component) boundary conditions (BCs) were applied at the inlet and

257 outlet (top and bottom). From the constant traction, the corresponding pressures and pressure

258 gradient were calculated. On the other four faces of the domain as well as on the solid-void

259 surfaces inside the porous medium, no-slip BCs were imposed (roughness was not accounted in

260 the model as the resolution of the SXCMT images cannot capture such features). More details on

261 the implementation of FEM and its BCs can be found in [59, 60]. The FEM simulation reproduced

262 the experimental conditions by matching all relevant experimental properties (e.g., viscosity) and

263 by adjusting the inlet and outlet pressure BCs until the average velocity matched the average

264 experimental pore water velocity of the column experiment.

265   In addition to flow rate and velocity profile convergence, confidence in the simulated

266 flow field was developed by calculating soil permeability using Darcy's law. The simulated

267 permeability (1.3×10^{-6} cm^2) is consistent with those experimentally determined for similarly

268 sized sands (e.g., 6.4×10^{-7} cm^2 [62]). However, it is important to note that this only ensures that the

269 average simulated flow properties are approximately consistent with the average experimental

270 flow. This was deemed sufficient as this study focuses on average behavior and does not

271 compare concentrations and simulated flow on a voxel-by-voxel basis.

272   It should be noted that no particle transport modeling was conducted. All estimates of

273   nanoparticle flux and flow in this paper are the result of combining the CFD modeled flow field

274   with the experimentally derived qSXCMT datasets of nanoparticle distribution.

Fluid Dynamics within the HSIC Geometry

275

276   An analytical solution was employed to solve for the fluid flow through the HSIC

277   geometry. The flow regime through this geometry is assumed to be creeping flow and is

278   described via the continuity and Stokes flow equations. The solution to the velocity vectors in the

279   HSIC geometry are not explicitly published in any of the mechanistic model papers [37, 38, 40, 48, 63].

280   However, the general stream function and HSIC-specific coefficients published in Elimelech [63]

281   can be used to solve for fluid velocities in the HSIC geometry.

Results

282

283   The results are divided into three sections. The first compares the HSIC geometry to the

284   pore and grain network extracted from the image-derived pore space. The second compares the

285   analytical solutions of fluid flow through the HSIC geometry to the CFD-simulated flow field in

286   the image-derived pore space. The third examines the distributions of nAg mass, mass *flux* and

287   mass flow in the SXCMT datasets. Throughout, the discussion considers whether the HSIC

288   geometry is appropriate for approximating nanoparticle transport through a realistic porous

289   medium.

HSIC vs. SXCMT pore and grain geometry

290

291   The computationally-determined porosity of the image-derived pore space (29%) is lower

292   than the experimentally-determined packed column porosity (33%), however the values are

293   similar enough that the computationally-determined SXCMT pore and grain statistics can be

294   taken as approximately equivalent to the experimental column's pore and grain network. The

295   computational grain and pore network statistics were compiled by examining 329 uniquely

296   identified grains, 2,139 pore bodies and 26,362 pore throats (the narrow region connecting two

297   pore bodies). The total number of grains and pores within the dataset is significantly larger (619

298   grains and 3,802 pores), however the extra grains and pores were excluded from the analysis as

299   they intersected the dataset edges. The aspect ratio of each grain was determined computationally

300   from the image-derived pore space by measuring the average ratio between the length of each

301   grain's longest axis to its shortest. The average grain aspect ratio was 1.64 suggesting that the

302   grains within the dataset were non-spherical which is qualitatively consistent with the images of

303   the SCXMT dataset in Figure S1 and with previously published literature [64] of typical sandy

304   media. The average pore inscribed radius is 59.4 μm and the average throat inscribed radius is

305   39.9 μm.

306   As mentioned, employing a CFT-HSIC mechanistic model (or η-correlation equation) to

307   describe nanoparticle transport assumes that all fluid flow occurs within the envelope

308   surrounding a spherical collector (illustrated in Figure S2 in the supplementary information).

309   The width of this fluid envelope (r, Figure S2) is defined so that the porosity of the HSIC

310   geometry (the volume ratio of fluid envelope volume/spherical collector volume) is equivalent to

311   the macroscopic porosity of the porous medium and is calculated from eq. 1:
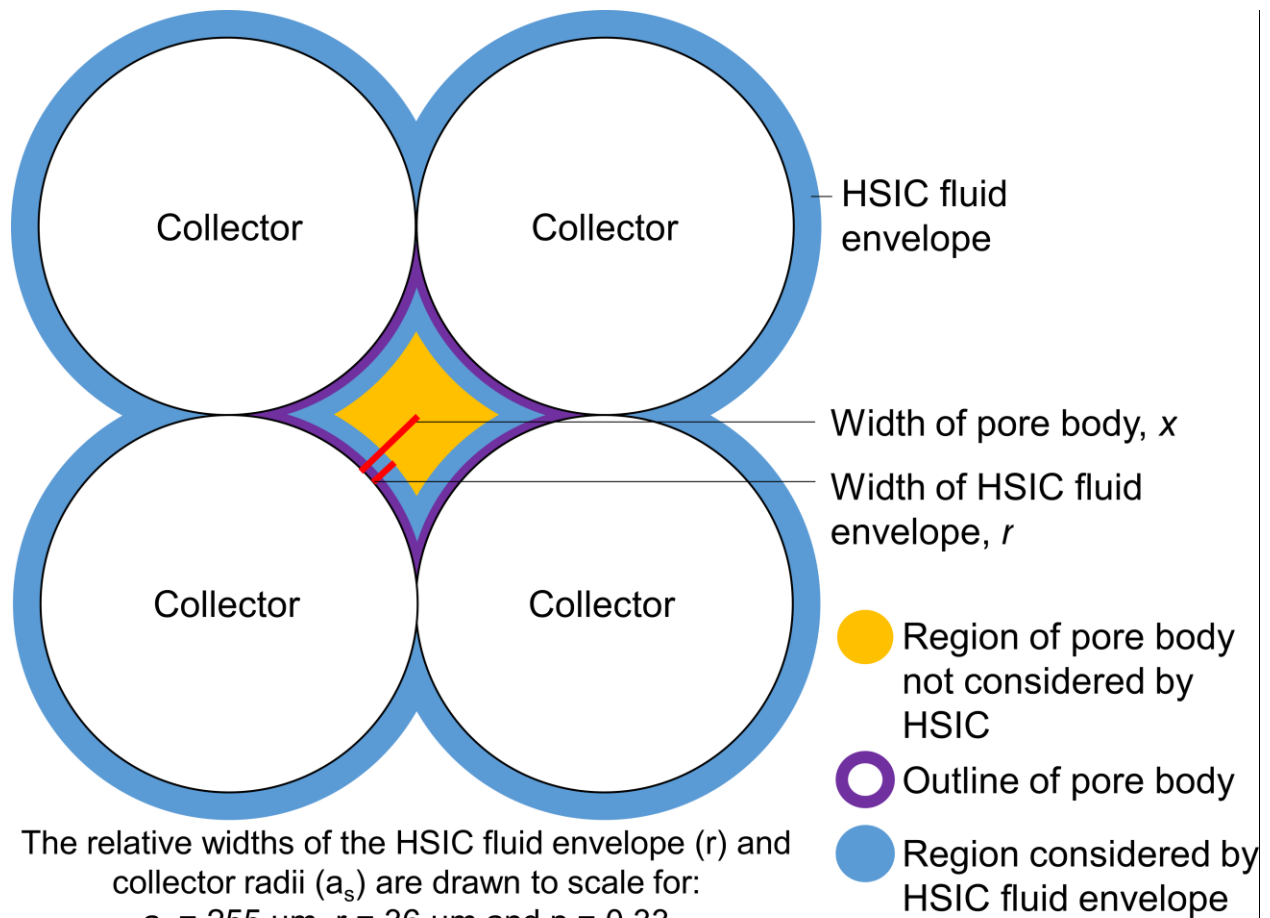
$$r = a_s(1-n)^{-1/3} - a_s$$
Eq. 1

312 where a_s is the radius of the spherical collector and n is the porosity. This definition of the fluid

313 envelope, along with eq. 1, is used throughout the CFT literature [37, 38, 40, 48, 63] as it is a relatively

314 simple method for accounting for porosity as well as the influence of neighbouring collectors on

315 the fluid velocity. Sieve analysis of the uniform quartz sand mixture determined the average

316 radius of the sand ($a_s = 255$ μm). Thus the HSIC geometry, applied to this experiment via eq. 1,

317 approximates all the pore space as being within a 36 μm-thick fluid envelop around the grain.

318 The HSIC envelope width (36 μm) is, in fact, more similar to the average pore throat

319 radius (39.9 μm) than the average pore body radius (59.4 μm). This suggests that a majority of

320 the uniquely identified pore bodies have some pore fluid volume that is at least 23 μm further

321 away from a grain surface than considered by HSIC. The difference between average pore body

322 width and HSIC fluid envelope width is illustrated by Figure 1.

323

The relative widths of the HSIC fluid envelope (r) and collector radii (a_s) are drawn to scale for:
a_s = 255 µm, r = 36 µm and n = 0.33

324

Figure 1: A depiction of how a pore body surrounded by a four circular collectors has a portion of pore space that is within the region considered by the HSIC's fluid envelope and a portion of pore space that is outside of the region considered by the HSIC fluid envelope.

The difference between the image-derived pore space's pore geometry and the HSIC is further highlighted by plotting the pore network and grain statistics as a cumulative percentage in Figure 2. The average Grain Effective Radius, 250 µm, was determined computationally from the image-derived pore space (defined as the average of the grain's short and long axis radii) and is consistent with the mean radius of sieved sand, 255 µm. It is also consistent, by extension, with the radius of the spherical collector in the HSIC geometry because the latter is set equal to the mean radius of sieved sand. The consistency between the HSIC collector radius and the average Grain Effective Radius suggests that (1) the image segmentation routine accurately

336   identified the boundary of the water/grain interface, and (2) the grains within the image-derived

337   pore space are representative of the overall experimental column. In addition, the distribution of

338   Grain Effective Radii within the image-derived pore space ranges from 200 – 300 μm (i.e., grain

339   effective diameter = 400 – 600 μm) and is consistent with the sieved grain size distribution (420

340   – 600 μm). The Grain Effective Radius tailing towards 0 μm in Figure 2 is likely due to the fact

341   that the cropping procedure for the network analysis could not remove all partial grains from the

342   statistics analysis.

343   The distribution of pore bodies in Figure 2 suggests that of the identified 2,139 pores,

344   approximately 80% have a radius equal to, or larger than, the width of the HSIC fluid envelope.

345   Thus within 80% of pores, some fraction of nanoparticles will be further away from the grain

346   surface than expected by CFT-HSIC models. The largest pore within the dataset has an inscribed

347   radii of 160 μm, therefore nanoparticles can be upwards of 124μm further away from a grain

348   surface than expected by CFT-HSIC. This trend is consistent with pore throats as well; of the

349   26,362 identified pore throats, approximately 50% are larger than the HSIC fluid envelope and

350   can range up to 130 μm in radius.

351
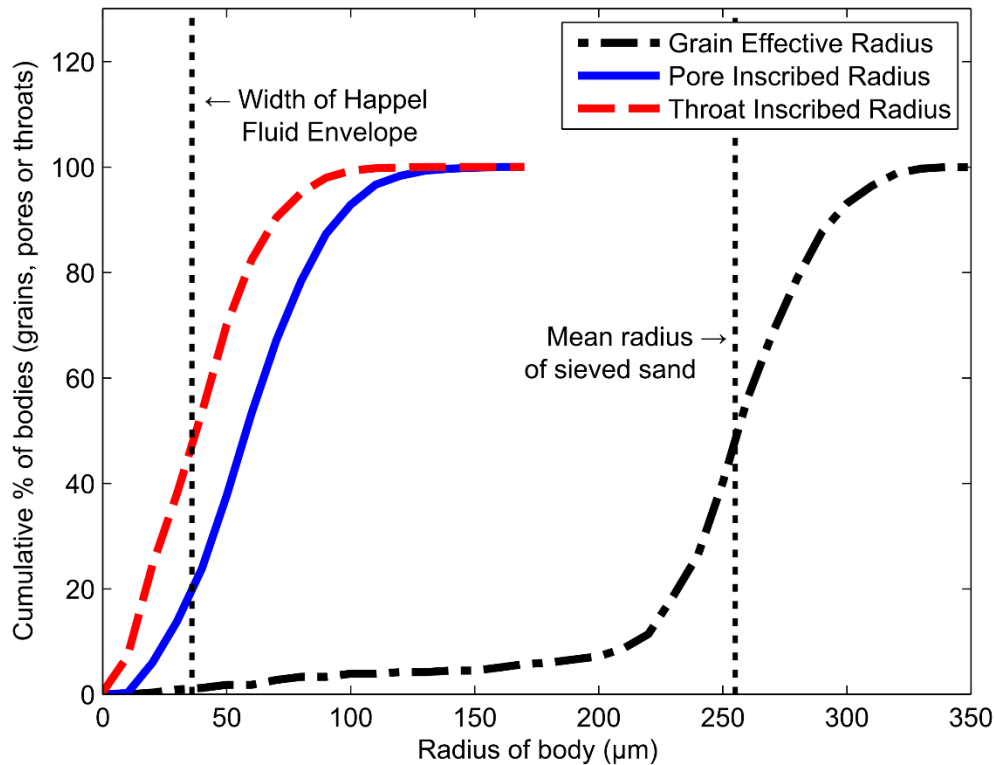
Figure 2: Cumulative size distributions of the grains (black), pores (blue) and pore throats (red)
within the pore network of the image-derived pore space. Inscribed radius refers to the radius of the
largest sphere that can be drawn entirely within the body. Effective radius is an average of the
inscribed radius and the length of the grain's longest axis.

356   Figure 3 (top) illustrates how the volume of pore space in the image-derived pore space

357   and HSIC geometry changes as a function of distance from the nearest grain surface. For the

358   image-derived pore space, after determining the distance between each pore space voxel and the

359   closest surface voxel, the distances were then sorted into bins representing 9.87 μm intervals

360   from the grain surface (corresponding to the length of 1 voxel). The number of voxels in each

361   bin was divided by the total number of pore space voxels to determine the percentage of pore

362   space within each bin. To determine the distribution of pore space in the HSIC geometry, the

363   volume of thin fluid shells were calculated in 9 μm intervals using the geometric equation for

364   volume of a sphere (9 μm intervals were used instead of 9.87 so that 4 data points would not

365   over-estimate the volume of HSIC pore space).

366   Figure 3 reveals that the volume of pore space in the image-derived pore space decreases

367   with distance from a grain surface, indicating that there is more pore space near the grain surface

368   than at the centers of the pores (qualitatively illustrated in Figure 1). This decreasing trend in the

369   real porous media is the opposite of what is encountered within the HSIC geometry. The trend

370   of increasing pore space volume with distance arises from the HSIC conceptual model; since the

371   volume of a sphere is a cubed function of its radius, the pore space volume in the HSIC geometry

372   is greatest at the outer edge of the fluid envelope. In Figure 3 (bottom), these trends are plotted

373   as a cumulative percentage of total pore space (total percentage of pore space closer to the grain

374   surface than a certain distance). It demonstrates that the cumulative distribution of the near-grain

375   pore space is similar between the image-derived pore space and the HSIC geometry. In fact, 50%

376   of all pore space in both the porous media and HSIC model is approximately 20-25 μm from a

377   grain surface. Figure 3 (bottom) highlights that 25% of the entire pore space is further away from

378   the grain than expected by the HSIC geometry. The difference in maximum pore size between

379   Figure 2 (maximum radius of pore body ~160 μm) and Figure 3 (distance to nearest grain surface

380   ~180 μm) is due to the fact that no cropping was performed for Figure 3.

381
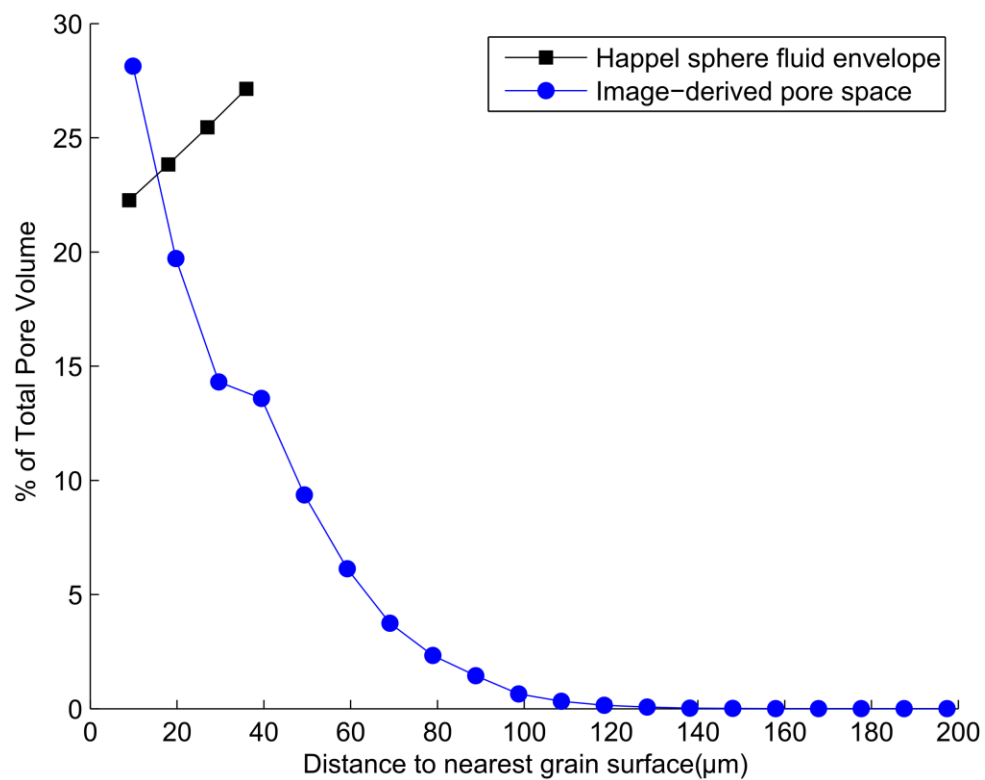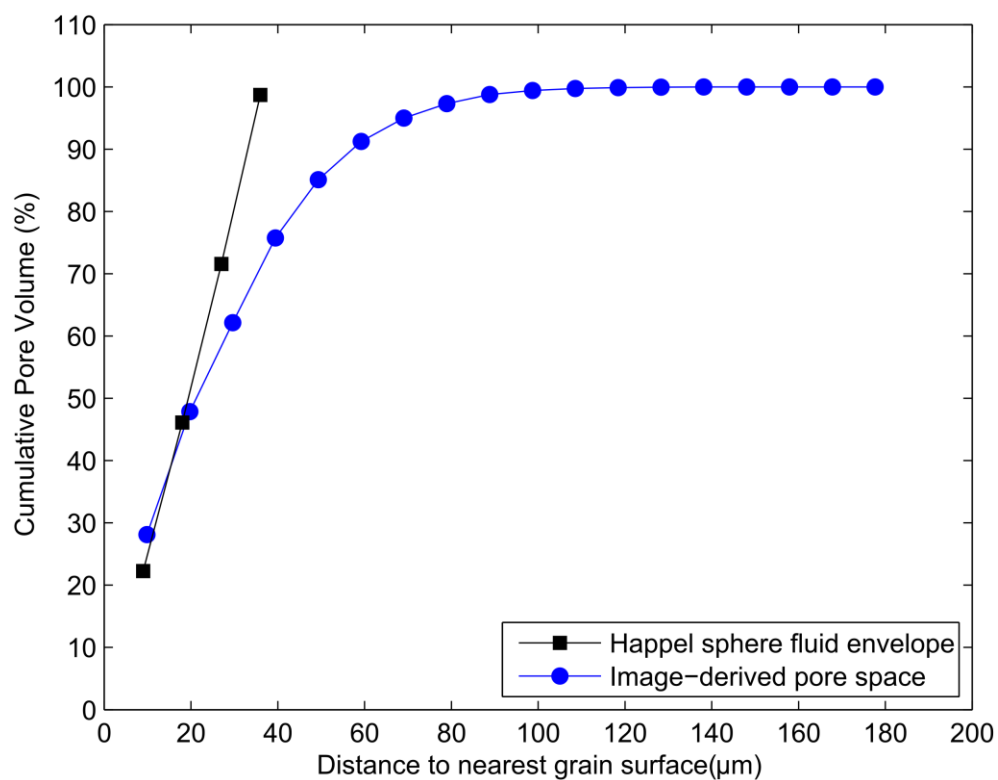
384 **Figure 3 (top)**: The percentage of pore space as a function of distance from the nearest grain surface for
385 the Happel sphere geometry (HSIC) (black squares) and the image-derived pore space (blue circle).

Figure 3 (bottom): The cumulative percentage of pore space as a function of distance from the nearest grain surface. Cumulative percentage refers to the sum of the geometries' pore space that is between the grain surface and a certain distance.

HSIC vs. SXCMT flow field

Averaging techniques were employed to analyze the CFD-simulated velocities in the image-derived pore space (see Figure 4 for a representative cross-section of velocity magnitude contours). The average pore water velocity around every grain in the image-derived pore space was plotted in Figure 4 (middle) as a function of distance from the nearest grain surface and angle from the downstream side of a grain (i.e. θ in Figure S2, measured from an axis parallel to the flow direction which passes through each grain's centroid). All voxels were sorted into 9.87 $\mu m \times 1°$ bins and averaged to calculate an average velocity for every definable distance and angle bin around a grain. Therefore, the colour mapped in each bin represents the average velocity within the image-derived pore space at that particular distance and angle. For the analytical solution for flow through the HSIC model, a similar process was used, the analytical solution was solved in increments of 9.87 μm and 1° and a nearest neighbor interpolation routine was used to generate a radial surface plot (Figure 4, right). The white spaces at the center of the graphs are not meant to represent the collector surface, but appear because distances are measured between voxel centroids and cannot be smaller than half a voxel length (representing the distance from a voxel face to the closest voxel centroid).
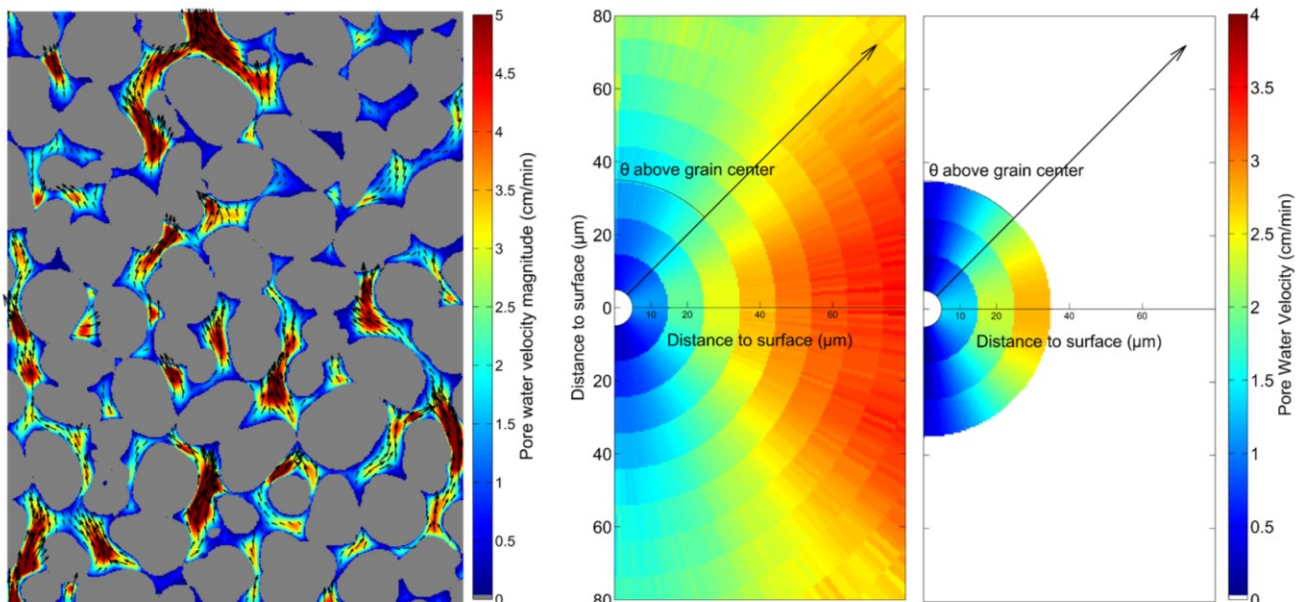
Figure 4 left: Contour plot of CFD-simulated pore water velocity magnitude overlain with black streamlines from a representative image-derived pore space cross-section. The direction of flow is upwards.

Figure 4 middle: Pore water velocity magnitude around the image-derived pore space. The direction of flow is upwards. Further details on this figure are discussed in text.

Figure 4 right: Pore water velocity magnitude around the HSIC geometry (right). The direction of flow is upwards. Further details on this figure are discussed in text.

The CFD-simulated flow field in the image-derived pore space illustrated in Figure 4 has a number of important features. Average velocity in the image-derived pore space is observed to be a function of angle with the highest velocities observed near the midpoint of the grain ($\theta = 90°$) and relatively low velocity regions near the upstream (bottom) and downstream (top) sides of the grain. The velocity distribution around the grain is also symmetric: the distribution on the upstream and downstream sides of the grains are similar for all distances. This indicates that there is little to no flow separation occurring on the downstream sides of the grains, which is consistent with the typical definition of creeping flow. The average velocity increases with distance from a grain surface with the highest velocities occurring in the centers of pores.

422 The flow field around the HSIC model (Figure 4, right) is in excellent qualitative

423 agreement with the CFD-simulated flow field in the image-derived pore space (Figure 4, middle)

424 within 36 μm of a grain's surface. The major velocity features in the image-derived pore space

425 are captured by the HSIC flow field, including the relatively low-velocity regions on the

426 upstream and downstream sides of the grains as well as the increase in velocity at $\theta = 90^\circ$ and the

427 symmetric flow behavior. However, the HSIC model under-estimates velocities in the upstream

428 and downstream regions (illustrated in Figure S3 and Figure 4); the velocities in the image-

429 derived pore space at 0° and 180° near 20 μm are higher than the velocities in the HSIC fluid

430 envelope. It is important to note that the above discussion compared the average flow velocity as

431 a function of distance irrespective of pore size. It has been previously shown that a range of fluid

432 velocities will occur even among similarly sized pores[65]. Thus the distribution of flow velocity at

433 a certain distance from a grain surface may vary between pores based on factors such as pore

434 connectivity, pore size, throat size and distribution of pore sizes [65]. The results in Figures 4

435 illustrate how these different flow distributions within each pore average out to yield a

436 distribution that is similar to a simple analytical flow solution. However, previous studies have

437 suggested that averaging flow fields in this manner may lose information vital to nanoparticle

438 transport such as immobile zones in soil [8, 65] or preferential flow pathways in size distributed

439 media[65].

440 To more quantitatively examine the distribution of velocities within the CFD-simulated

441 image-derived pore space, Figure 5 plots the velocity distribution in Figure 4 as a one-

442 dimensional function of distance to the nearest grain where the velocity was averaged over all

443 angles for each particular distance interval with error bars representing the maximum and

444 minimum values of velocity at each distance. Confirming the trend observed in Figure 4, the

445   average CFD-simulated and HSIC analytical velocities are very similar within the region

446   encompassed by the HSIC. Outside of the HSIC region, the average pore water velocities within

447   the centers of the largest pores (~100 μm) may be as large as 2× the overall average pore water

448   velocity (1.38 cm/min). This trend is qualitatively consistent with the velocity contour plot

449   illustrated in Figure 4 (left). Even within the HSIC region, the box and whisker plot in Figure 5

450   show that the individual values of CFD-simulated velocity can be upwards of 20 times larger

451   than within the HSIC model at identical distances from grain surfaces. Overall, these results

452   suggest that nanoparticles may be experiencing significantly higher fluid velocities than expected

453   within the CFT-HSIC model. These larger-than-expected velocities will yield forces and torques

454   on the nanoparticles that are outside the range considered by the CFT-HSIC mechanistic model.

455   To the best of the authors' knowledge this represents one of the first comparisons between CFD-

456   simulated velocities in a real sand and the HSIC model.

457

458
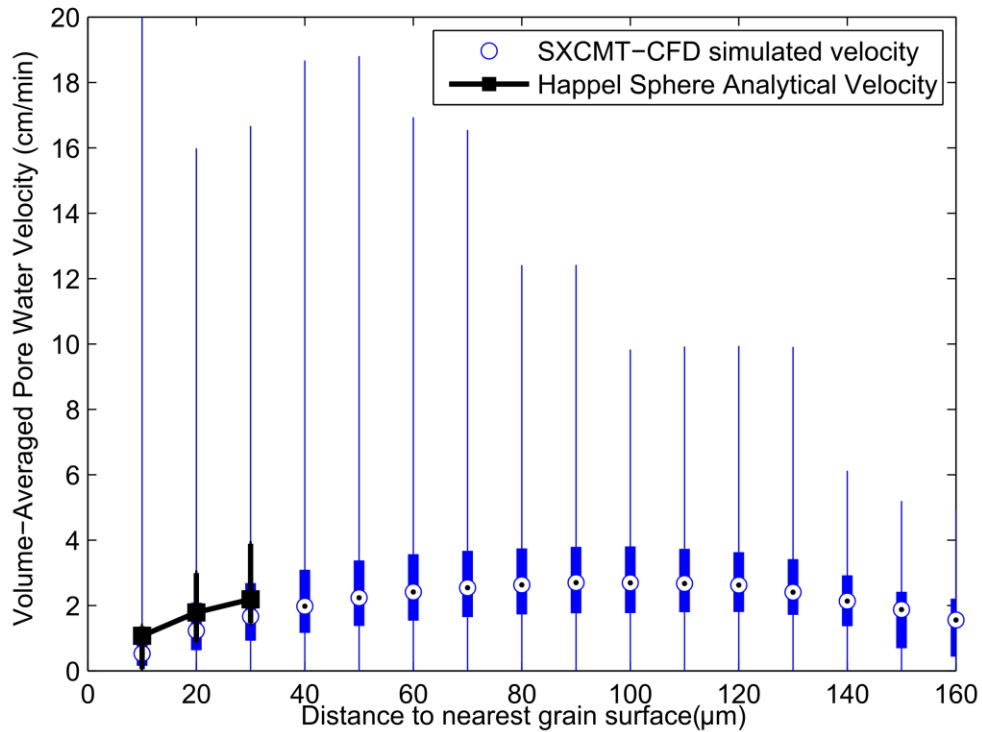
Figure 5: The average pore water velocity magnitude as a function of distance from the nearest grain
surface for both the HSIC geometry (black squares) and the image-derived pore space (blue circles with
a black dot). The velocity contours presented in Figure 4 were employed to create this plot; at each 9.87
µm distance interval the velocities were averaged over all 1º bins (i.e., each datapoint represents
velocity averaged over 0 – 180 º) and weighted by the fraction of pore volume in each 1 º bin. The
SXCMT-CFD simulated velocity distribution is presented as a box-and-whisker plot where the bounds of
the boxes represent the 25% and 75% quartile at each distance and the length of the whiskers
represents the minimum and maximum velocity at each distance. The error bars on the Happel Sphere
Analytical Velocity profile represents the maximum and minimum velocities at each distance from the
grain surface.

469

470

471

472

Nanoparticle mass distribution in qSXCMT datasets

473

474   Figure 6 presents the distribution of nanoparticle mass within the qSXCMT dataset as a

475 function of distance to the nearest grain surface for each imaged time-step. The mass distribution

476 curves were calculated by first determining the nanoparticle mass in each voxel, calculated by

477 multiplying each voxel's qSXCMT-determined concentration by the volume of the voxel

478 (approximately 961.5 μm^3). This calculation was repeated for every voxel > 17.3µm from a grain

479 surface (i.e., outside the shadow zone). The distance between every pore space voxel and the

480 nearest grain surface in each qSXCMT dataset was measured and sorted into 9.87 µm intervals.

481 The nanoparticle mass in each interval was plotted as a function of mass versus distance to the

482 nearest surface (Figure 6, top).

483   As illustrated in Figure 6 (top), most nanoparticle mass is located near the grain surface;

484 this is expected as the near surface regions possess the largest volume of pore space (shown in

485 Figure 3). While the qSXCMT method is currently unable to quantify nanoparticle mass closer

486 than 17.3 µm (25% of the total pore space, Figure 3), based on the trend in Figure 3, it is

487 hypothesized that, in general, the total mass of nanoparticles continues increasing with

488 decreasing distance to the grain surface. The term 'quantifiable mass' is used throughout this

489 section to refer to mass, or mass flow, outside of the 'shadow zone' that can be quantified via the

490 qSXCMT procedure.

491   The general shape of the mass distribution curve in Figure 6 (top) approximates the shape

492 of the pore space volume curve in Figure 3 (top). To quantitatively compare the distributions of

493 mass and volume, Figure 6 (bottom) plots the cumulative percentage of quantifiable nanoparticle

494 mass as a function of distance to the nearest grain surface. This represents the total percentage of

495   quantifiable nanoparticle mass that is closer to the grain surface than a certain distance. Figure 6

496   suggests that, at every time-step, only approximately 60% of all quantifiable nanoparticle mass is

497   within the fluid region encompassed by the HSIC fluid envelope.

498   Figure 3 can be employed to estimate the nanoparticle mass distribution in the 'shadow

499   zone' region, which accounts for 25% of all pore space voxels. Assuming a strictly per-volume

500   ratio, 75% of the total nanoparticle mass can be quantified via qSXCMT at each time step.

501   Incorporating this into the cumulative percentages in Figure 6 (bottom) yields an adjusted

502   estimate of approximately 70% of total nanoparticle mass within the HSIC fluid envelope region

503   with 30% of nanoparticle mass outside of the envelope. The percentage of nanoparticle mass

504   outside the envelope is greater than the percentage of pore volume outside the envelope. This

505   indicates that nanoparticles are not uniformly distributed throughout the pore space and that the

506   pore-scale concentration gradients identified by Molnar et al. [8] significantly affect the overall

507   mass distribution through the pore space. It should be noted that while this distribution is for

508   nanoparticle mass in an 'unfavorable' deposition scenario, a previous study conducted on this

509   same dataset concluded that the presence of a repulsive energy barrier had no observable impact

510   on the pore-scale distribution of nanoparticle concentration at the scale examined in Figure 6[8].

511

512

513

514
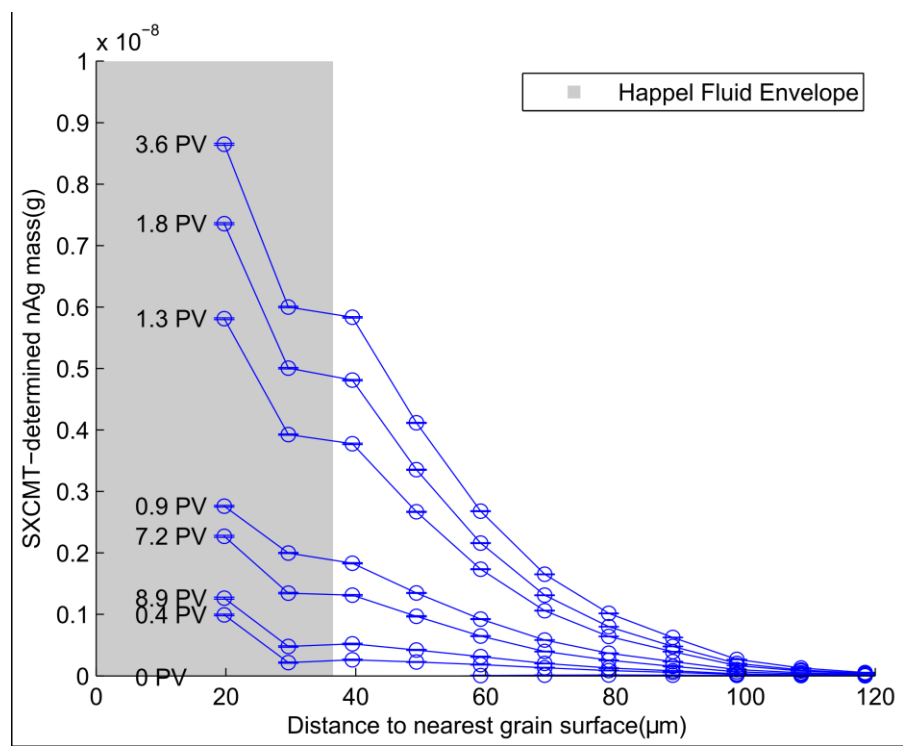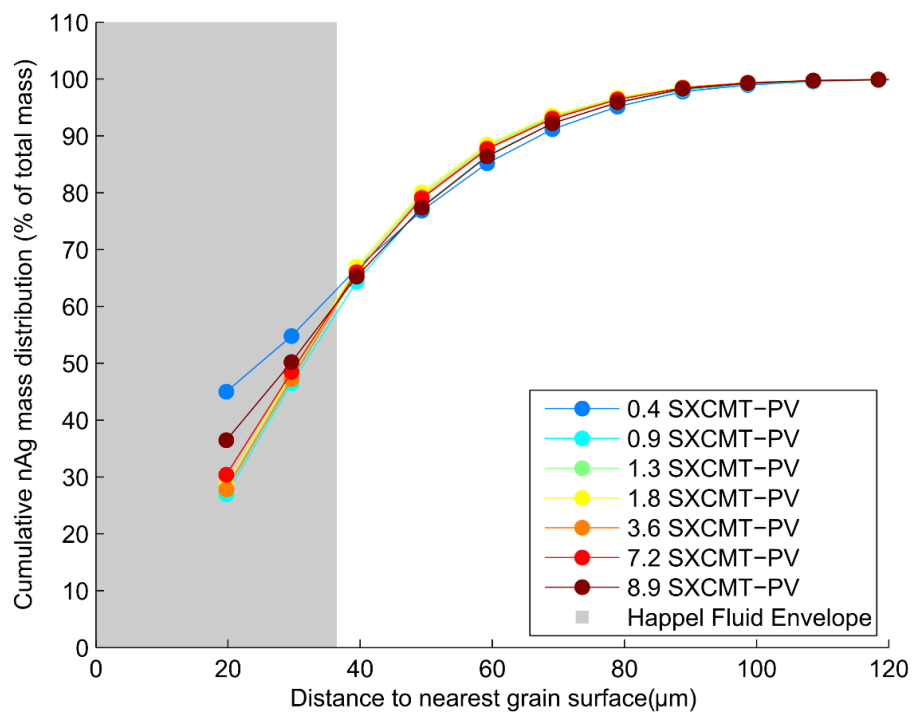
Figure 6 (top): The qSXCMT-determined nAg mass plotted as a function of distance from the nearest grain surface (top) for each imaged time-step. The gray box represents the thickness *r* of the HSIC fluid envelope. To avoid cluttering the figure, 'PV' is used instead of 'SXCMT-PV's'. The error bars on the qSXCMT dataset lines represent 95% confidence intervals calculated at each datapoint. Every datapoint in the qSXCMT dataset has an error bar, however the error bars may be smaller than the size of the data point marker and not visible.

Figure 6 (bottom): The cumulative percentage of qSXCMT-determined nAg mass for each imaged time-step as a function of distance from the nearest grain surface. Cumulative percentage refers to the total percentage of nAg mass that is between the grain surface and a certain distance from the surface.

The 1-dimensional (1-D) CFD flow field and the 1-D distribution of nanoparticle mass were combined to estimate the 1-D averaged nanoparticle advective mass *flux* rates (mass flow of nAg per unit area). This analysis was conducted to develop an understanding of how close advective flow through a realistic 3-dimensional porous media domain will bring nanoparticles to a collector surface, as such no diffusive flux was considered in this analysis. Calculations of the maximum possible change in concentration due to diffusive flux indicates that diffusive flux is negligible compared to the estimated advective flux rates. The estimated 1-D nanoparticle mass *flux* are plotted as a function of distance to the nearest grain surface. The 1-D concentration distribution was calculated by dividing the mass distribution in Figure 6 by the distribution of pore space in Figure 3, which yields an average concentration value for each binned distance from a grain surface. The 1-D CFD velocity magnitude plot in Figure 5 was separated into its component velocities (v_x, v_y and v_z), each of these 1-D distributions of component velocities was multiplied by the 1-D concentration distribution to estimate mass *flux* distributions in the x, y and z directions (q_x, q_y and q_z). These component mass *flux* distributions were summed to determine an overall mass *flux* distribution ($q = q_x + q_y + q_z$) as a function of distance to the nearest grain surface. This mass *flux* distribution is illustrated in the supporting material (Figure S4).

541   Due to the high velocities and higher concentrations in the centers of the larger pores,

542   mass *flux* rates were the highest at the centers of the pores for the time-steps between 0.9 and 3.6

543   SXCMT-PV's and, to a lesser extent, 7.2 SXCMT-PV. The mass *flux* rates do not appreciably

544   change with distance from the grain surface for the early time-step 0.4 SXCMT-PV and the last

545   time-step 8.9 SXCMT-PV; this is likely due to the minimal concentration gradients noted by

546   Molnar et al. [8] at these times.

547   The average mass *flux* distributions were employed to estimate the total quantifiable

548   nanoparticle mass flow rate distribution. Component mass flow rates in the x, y and z directions

549   (Q_x, Q_y and Q_z) were estimated by multiplying the distribution of component mass *flux* rates (q_x,

550   q_y and q_z) by the number of voxels within each 9.87 μm distance interval and by the area of a

551   voxel face (9.87×9.87 μm). The component mass flow rates were then summed to yield the

552   nanoparticle mass flow rate distribution ($Q = Q_x + Q_y + Q_z$) in Figure 7.

553   Figure 7 (top) represents the quantifiable mass flow as a function of distance from the

554   grain surface and is qualitatively different from the distribution of pore space. The nanoparticle

555   mass flow rate exhibits a bi-modal distribution with one peak near the grain surface and a second

556   peak at a distance of 40 μm. The location of this second peak mass flow rate was unexpected as

557   it does not occur at a region of peak nanoparticle mass, mass *flux* or fluid velocity. This second

558   peak is likely due to a combination of several factors including nanoparticle concentration

559   distribution, fluid velocity distribution, the distribution of small, medium and large pores

560   illustrated in Figure 2 and the overall distribution of pore space illustrated in Figure 3. This bi-

561   modal peak is not attributed to the presence of a repulsive energy barrier as it was previously

562   shown that unfavorable conditions do not impact the distribution of pore-scale nanoparticle

563   concentrations at the scales examined here[8].

564   Figure 7 (bottom) plots the cumulative percentage of quantifiable nanoparticle mass flow

565   as a function of distance to the nearest grain surface. The cumulative percentage at the edge of

566   the HSIC fluid envelope can be used to compare the distributions of pore space volume,

567   nanoparticle mass and mass flow. Accounting for the pore space volume within the 'shadow

568   zone' in the same manner as the mass distribution (Figure 6) discussed above, approximately

569   37% of total nanoparticle mass flow is occurring further away from the grain surface than

570   considered by the HSIC model. Moreover, more mass flow is occurring further away from the

571   grain surface than would be expected by either the proportion of pore space (25%) or

572   nanoparticle mass (30%) outside of the envelope. The distribution of velocity in Figure 5 is

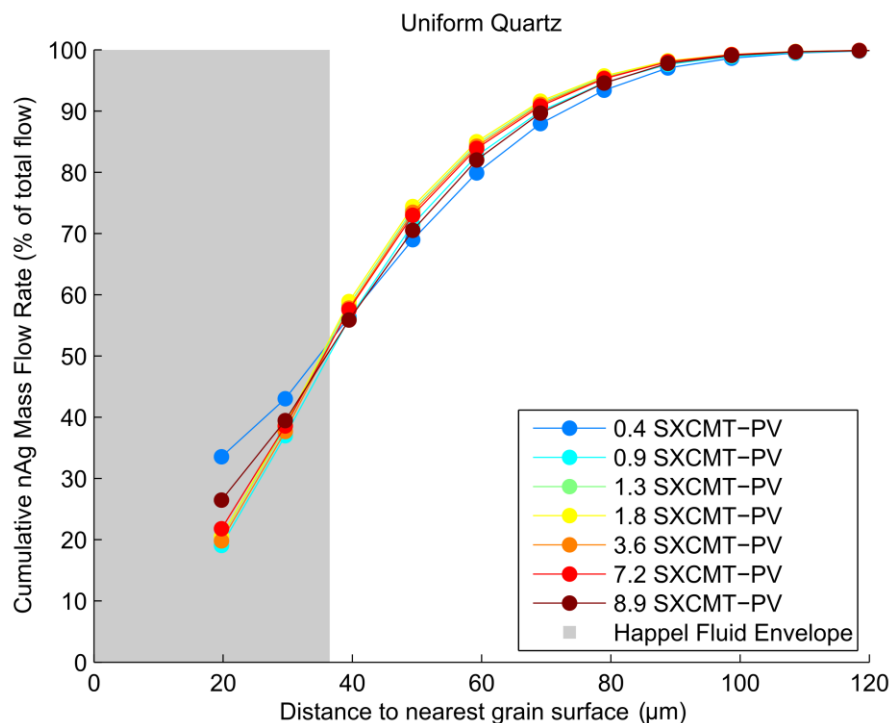573   responsible for the mass flow that favours the centers of pores.

574

575

576

577

578
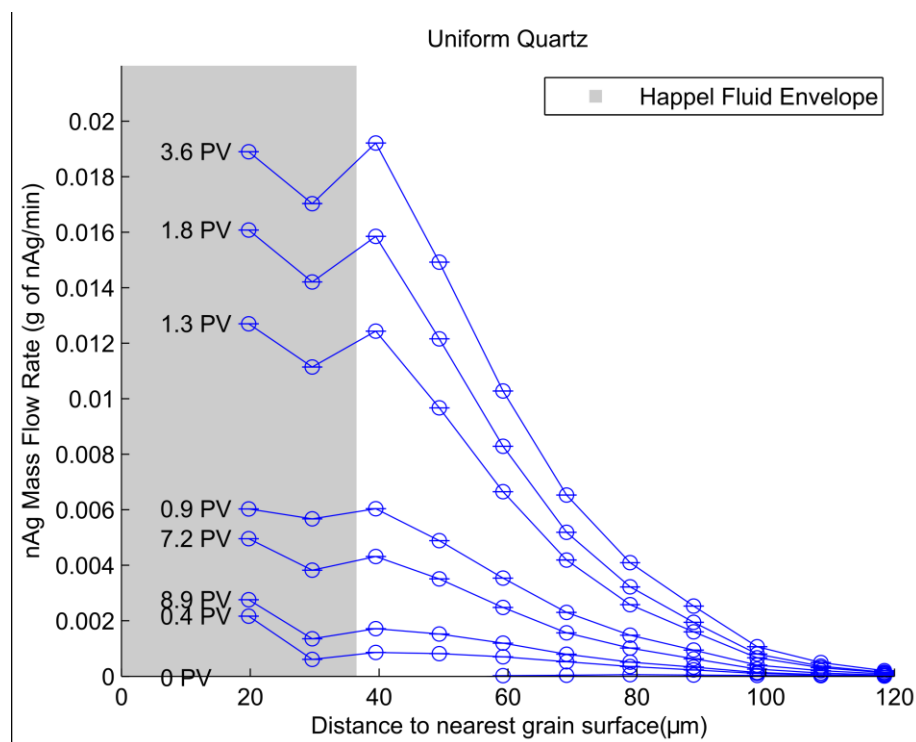
Figure 7 (top): The estimated nAg mass flow rate as a function of distance from the nearest grain surface for each imaged time-step. The gray box represents the thickness *r* of the HSIC fluid envelope. To avoid cluttering the figure, 'PV' is used instead of 'SXCMT-PV's'.

Figure 7 (bottom): The cumulative percentage of estimated nAg nanoparticle mass flow for each imaged time-step as a function of distance from the nearest grain surface. Cumulative percentage refers to the total percentage of nAg mass flow occurring between the grain surface and a certain distance from the surface.

Discussion

These results indicate that the HSIC geometry results in a 'compression' of the actual

pore space; it is hypothesized that this may be impacting the accuracy of CFT-HSIC's

predictions for nanoparticle transport. The trends in pore size and pore space highlighted in

Figures 4 and 5 suggest that the HSIC model, purely on the basis of pore geometry, will treat

flow and transport processes as being closer to the grain surface than they would be within

medium-to-larger pores in the qSXCMT dataset. Thus flow and transport processes such as the

593 diffusive flux of nanoparticles towards a grain surface, which could be occurring upwards of 197

594 μm away, the maximum distance from a grain surface identified within the qSXCMT datasets,

595 will be treated by HSIC as being within 36 μm of a grain surface. Approximately 80% of all

596 uniquely identified pore bodies are affected by this pore space compression, and 25% of the total

597 pore space in the qSXCMT-dataset is treated by the HSIC geometry as being closer to a grain

598 surface than it actually is. Given the similarities in grain shape between this study and a previous

599 study [64], this trend is likely widely present in sandy media.

600   Figures 6 and 7 indicate that large percentages of nanoparticle mass (30%) and mass flow

601 (37%) are further away from the grain surface than is considered by the HSIC model. These

602 percentages remain consistent for all time-steps through the transport experiment. The degree to

603 which CFT's prediction of colloid retention is affected by these percentages depends on the

604 process governing colloid transport. Micron-sized colloids rely on interception (commonly

605 denoted by η_I) to contact the grain surface e.g. [36, 37]. Interception is when colloids are flowing

606 along a streamline which passes within 1 colloid radius of the collector surface and contact the

607 surface by virtue of their size. The micron-sized colloids exhibit a minimal degree of Brownian

608 motion – diffusion of particles arising from collisions with surrounding molecules – and are not

609 expected to diffuse across a significant number of streamlines. This strong interception behavior,

610 coupled with weak diffusive transport, suggests that in the absence of gravitational settling only

611 colloids on specific trajectories will be contacting and attaching to the collector; the 'critical

612 trajectory' refers to the trajectory beyond which colloids will no longer intercept the grain

613 surface. Rajagopalan and Tien [37] employ this concept to simplify their calculations by only

614 considering colloids within the critical trajectory. As a result, the accuracy of CFT for micron-

615 size colloid transport and retention will depend on how well the modeled geometry captures the

616 streamlines within a realistic medium. Geometry simplifications will adversely impact the

617 accuracy of streamlines within CFT models. However, the good agreement between the

618 analytical HSIC and CFD-simulated flow fields (Figure 4) suggests that, on average, the near-

619 surface flow field through the image derived pore space (<36 μm from a collector surface) is

620 approximated reasonably well by the HSIC model. This result, in combination with the strong

621 interception and weak diffusive behaviour of micron-sized colloids, suggests that this geometry

622 can be appropriate for predicting micron-sized colloid retention rates. This may be a reason for

623 why micron-sized particle behaviour has been shown to be accurately modelled by CFT-HSIC

624 models[38], however trajectory simulations of micron-sized colloids are needed to confirm this

625 hypothesis.

626   However, interception is not a dominant mechanism for nanoparticles. Due to

627 nanoparticles' small radii there are only a small number of trajectories which will bring

628 nanoparticles within 1 colloid radius of the collector. For nanoparticles, diffusion is the main

629 mechanism for contacting collector surfaces (commonly denoted by η_D)[46]. The fraction of

630 nanoparticles diffusing distances of $0 - 36$ μm across the HSIC envelope will be much larger

631 than in the porous medium where diffusive distance can range from $0 - 197$ μm (the maximum

632 distance from a grain surface in the image-derived pore space) . Given these results showing a

633 substantial mass flow of nanoparticles is further away from the grain surface than expected by

634 HSIC, approximating all nanoparticles as being within the 36μm HSIC envelope is expected to

635 cause the model to over-estimate η and nanoparticle retention rates. This is hypothesized to be a

636 reason that HSIC-CFT models typically over-predict η and k_{att} [8, 38, 46].

637   The results presented in Figure 2, 5, 6 and 7 suggest that nanoparticle transport studies

638 which employ η-correlation equations from CFT to estimate η e.g., [24, 25, 26, 27, 28, 29, 30, 31, 32, 33, 34, 35]

639   are over-predicting η due to the CFT-HSIC geometry's inability to consider nanoparticle mass

640   flow outside the fluid envelope. It should be noted that, as this study does not employ a

641   mechanistic particle tracking model for trajectory analysis, the proposed link between

642   nanoparticle mass flow outside the Happel envelope and CFT over-prediction remains a

643   hypothesis and should be considered an open research question. CFT models are starting to

644   employ alternative geometries such as the Hemisphere-in-Cell model [66], cylindrical pore model[67]

645   and the randomly packed collector model [46, 68], however it is unknown if these geometries will

646   overcome the limitations of the HSIC geometry in predicting nanoparticle retention. Many of

647   these alternative geometries are highly tunable and, as such, are promising potential avenues for

648   trajectory analysis and exploring the link between compressed pore space and CFT over-

649   prediction of nanoparticle attachment.

650   For nanoparticle transport, it is expected that the accuracy of a mechanistic CFT model is

651   linked to how well its geometry mimics the distribution of pore space, and the range of diffusive

652   distances required to reach a grain surface, found in realistic porous media. Nelson and Ginn [38]

653   examined this link; they compared the relative accuracy of 5 different mechanistic CFT models

654   with different geometries of which 3 employed the HSIC[37, 38, 40], 1 employed a random sphere

655   packing[46], 1 employed a 'Hemisphere-in-Cell' model [41, 43, 69, 70, 71]. While their results suggested

656   no observable correlation between geometry realism and accuracy, the 5 models incorporated

657   different flow fields, force-torque balances and different treatments of Brownian motion [4] which

658   makes it impossible to compare the accuracy of those models solely on the basis of geometry.

659   Further study is required to examine the link between geometry realism and model accuracy. Of

660   note is the 'Hemisphere-in-Cell' model which includes concentric fluid envelopes around each

661   hemisphere in a manner similar to the HSIC model, but also incorporates a simplified force

662 balance for colloids outside of the fluid envelope [70] and a pendular ring [43] for the express purpose

663 of adding a small volume of pore space at slightly further distances from the grain surface. While

664 these additions are unlikely to encapsulate the full range of diffusive distances observed in

665 Figure 7, they do bring a degree of increased realism to a unit-cell model and could thereby

666 potentially improve predictions for nanoparticle attachment.

667 In favorable DLVO conditions where $\alpha = 1$ (i.e., attachment efficiency = 1) this over-

668 prediction of η will result in over-predictions of the nanoparticle kinetic retention rate coefficient

669 k_{att} and over-predictions of the overall rate of nanoparticle retention. This may result in under-

670 predictions of nanoparticle mobility and risk to nearby drinking water supplies. In unfavorable

671 DLVO conditions where $\alpha < 1$, a-priori estimations of η are required to accurately determine α.

672 CFT-HSIC over-predictions of η will then result in under-estimations of α. Numerous studies

673 have tried to identify trends in nanoparticle α [1, 29, 32, 72, 73, 74, 75] but with generally limited success.

674 This limited success in describing α for nanoparticle transport may be due, in part, to the

675 inability to accurately predict η with CFT-HSIC mechanistic models and correlation equations.

676 The pore-scale distribution and behavior of nanoparticles within real porous media is

677 currently poorly understood [4], so it is unclear the degree to which the extended diffusive

678 distances (0–36 μm vs 0–197 μm) contribute to over-predicted retention rates as opposed to other

679 proposed mechanisms (e.g., immobile zones) [8]. Further research is required to determine how

680 fluid and nanoparticle parameters (e.g., particle size, viscosity), as well as different types of

681 porous media (e.g., geometry, surface properties) influence the 'diffusive error' arising from

682 compressing larger pore bodies into thin HSIC fluid envelopes.

683 # Summary and Conclusions

684   Pore-scale silver nanoparticle distributions were imaged via quantitative Synchrotron X-

685   ray Computed MicroTomography (qSXCMT) and linked with Computational Fluid Dynamics

686   simulations of fluid flow through the imaged pore space. This examination yielded some of the

687   first ever quantitative evaluation of pore-scale nanoparticle transport through a real porous

688   medium. Summarized findings include: (1) The pore space ranged from $0 - 197$ μm from a grain

689   surface, of which 25% was further from the grain than the 36 μm fluid envelope assumed by the

690   HSIC model; (2) Average pore velocity, which is a function of distance from the grain surface,

691   agreed well between the experiment and HSIC model within the HSIC fluid envelope; however,

692   the former were 2 times larger than the latter in the centers of the larger pores; (3) The individual

693   values of CFD-simulated velocity were upwards of 20 times those of the HSIC model at identical

694   distances from grain surfaces; and (4) Approximately 30% of all nanoparticle mass and 37% of

695   all nanoparticle mass flow occur further away from the grain surface than expected by the HSIC

696   geometry. While it is generally widely acknowledged that the Happel Sphere model is a

697   simplification of real porous media systems, this paper is one of the first studies that provides a

698   detailed examination of which components of real porous media are simplified specifically with

699   respect to nanoparticle transport. Overall, this work suggests that the HSIC geometry

700   assumptions are unnaturally compressing the pore space around the Happel sphere. It is

701   therefore hypothesized that a significantly lower fraction of nanoparticles will contact a grain

702   surface by diffusion than expected by HSIC geometry. Moreover, it is hypothesized that this

703   difference between reality and model, termed 'diffusive error', is likely contributing to CFT-

704   HSIC's typical over-predictions of η for nanoparticles. This study also confirms that, despite

705   these simplifications, the average pore space distribution and the average velocity distribution

706   within 36μm of a grain surface are well represented by the HSIC geometry.

707   We acknowledge that we only examined nanoparticle transport through one soil sample

708   (a relatively uniform quartz sand), so the results from this study – such as the percentages of

709   nanoparticles outside the HSIC fluid envelope –are specific to the grain and pore distribution in

710   the examined qSXCMT datasets as well as the experimental fluid velocity. In addition, this study

711   only examined unfavorable conditions. However, these results are not expected to be sensitive to

712   grain surface chemistry/DLVO interactions as the distances examined within this study are

713   orders of magnitude larger than the scale at which DLVO interactions are significant. In addition,

714   Molnar et al. [8] noted that the concentration gradients within a pore did not change between

715   unfavorable and favorable deposition conditions. These limitations do not alter the findings of

716   this study, that a significant fraction of nanoparticles are further away from the grain surface than

717   considered by standard CFT models. It should be noted that the implications of this finding, a

718   proposed link between the compressed pore space in HSIC and over-prediction of nanoparticle

719   attachment by CFT, remains a hypothesis and should be considered a valuable avenue for future

720   research. Future work on this topic should include modifying existing CFT geometries such as

721   the HSIC or Hemisphere geometry, or developing new geometries, and employing trajectory

722   analysis with a mechanistic model to further evaluate the hypothesis and quantify the impact of

723   the compressed pore space on CFT predictions of collector efficiency . In addition, future work

724   should pay specific attention to developing CFT geometries and models that are appropriate for

725   nanoparticle transport and consider the full range of pore sizes that are present. Future work on

726   this topic should also examine the results presented in this study for a range of porous media and

727   nanoparticle types. Research on nanoparticle-specific CFT geometries has begun (see [46, 68]) and

728   further developing these models and concepts should be considered a promising avenue of

729   research.

Acknowledgements

740

741   References

742

743   1.   Petosa, A. R.; Jaisi, D. P.; Quevedo, I. R.; Elimelech, M.; Tufenkji, N. Aggregation and Deposition
744 of Engineered Nanomaterials in Aquatic Environments: Role of Physicochemical Interactions. *Environ.*
745 *Sci. Technol.* **2010,** *44* (17), 6532-6549.
746   2.   O'Carroll, D.; Sleep, B.; Krol, M.; Boparai, H.; Kocur, C. Nanoscale zero valent iron and bimetallic
747 particles for contaminated site remediation. *Adv. Water Resour.* **2013,** *51* (0), 104-122.
748   3.   Goldberg, E.; Scheringer, M.; Bucheli, T. D.; Hungerbühler, K. Critical Assessment of Models for
749 Transport of Engineered Nanoparticles in Saturated Porous Media. *Environ. Sci. Technol.* **2014,** *48* (21),
750 12732-12741.
751   4.   Molnar, I. L.; Johnson, W. P.; Gerhard, J. I.; Willson, C. S.; O'Carroll, D. M. Predicting colloid
752 transport through saturated porous media: A critical review *Water Resour. Res.* **2015,** *51* (50th
753 anniversary special collection), 6804-6845.
754   5.   Jiang, X.; Tong, M.; Kim, H. Influence of natural organic matter on the transport and deposition
755 of zinc oxide nanoparticles in saturated porous media. *Journal of Colloid and Interface Science* **2012,** *386*
756 (1), 34-43.
757   6.   Jiang, X.; Tong, M.; Lu, R.; Kim, H. Transport and deposition of ZnO nanoparticles in saturated
758 porous media. *Colloids and Surfaces A: Physicochemical and Engineering Aspects* **2012,** *401* (0), 29-37.
759   7.   Uyusur, B.; Darnault, C. J. G.; Snee, P. T.; Koken, E.; Jacobson, A. R.; Wells, R. R. Coupled effects
760 of solution chemistry and hydrodynamics on the mobility and transport of quantum dot nanomaterials
761 in the vadose zone. *Journal of Contaminant Hydrology* **2010,** *118* (3-4), 184-198.

762   8.   Molnar, I. L.; Gerhard, J. I.; Willson, C. S.; O'Carroll, D. M. The impact of immobile zones on the
763   transport and retention of nanoparticles in porous media. *Water Resour. Res.* **2015**.
764   9.   Kanel, S.; Flory, J.; Meyerhoefer, A.; Fraley, J.; Sizemore, I.; Goltz, M. Influence of natural organic
765   matter on fate and transport of silver nanoparticles in saturated porous media: laboratory experiments
766   and modeling. *J. Nanopart. Res.* **2015,** *17* (3), 1-13.
767   10.   Joo, S. H.; Al-Abed, S. R.; Luxton, T. Influence of Carboxymethyl Cellulose for the Transport of
768   Titanium Dioxide Nanoparticles in Clean Silica and Mineral-Coated Sands. *Environ. Sci. Technol.* **2009,** *43*
769   (13), 4954-4959.
770   11.   Lanphere, J. D.; Luth, C. J.; Walker, S. L. Effects of Solution Chemistry on the Transport of
771   Graphene Oxide in Saturated Porous Media. *Environ. Sci. Technol.* **2013,** *47* (9), 4255-4261.
772   12.   Liang, Y.; Bradford, S. A.; Simunek, J.; Vereecken, H.; Klumpp, E. Sensitivity of the transport and
773   retention of stabilized silver nanoparticles to physicochemical factors. *Water Research* **2013,** *47* (7),
774   2572-2582.
775   13.   Liang, Y.; Bradford, S. A.; Simunek, J.; Heggen, M.; Vereecken, H.; Klumpp, E. Retention and
776   Remobilization of Stabilized Silver Nanoparticles in an Undisturbed Loamy Sand Soil. *Environ. Sci.*
777   *Technol.* **2013,** *47* (21), 12229-12237.
778   14.   Wang, D.; Ge, L.; He, J.; Zhang, W.; Jaisi, D. P.; Zhou, D. Hyperexponential and nonmonotonic
779   retention of polyvinylpyrrolidone-coated silver nanoparticles in an Ultisol. *Journal of Contaminant*
780   *Hydrology* **2014,** *164* (0), 35-48.
781   15.   Wang, Y.; Li, Y.; Costanza, J.; Abriola, L. M.; Pennell, K. D. Enhanced Mobility of Fullerene (C60)
782   Nanoparticles in the Presence of Stabilizing Agents. *Environ. Sci. Technol.* **2012,** *46* (21), 11761-11769.
783   16.   Wang, Y.; Li, Y.; Fortner, J. D.; Hughes, J. B.; Abriola, L. M.; Pennell, K. D. Transport and Retention
784   of Nanoscale C60 Aggregates in Water-Saturated Porous Media. *Environ. Sci. Technol.* **2008,** *42* (10),
785   3588-3594.
786   17.   Wang, D.; Zhang, W.; Zhou, D. Antagonistic Effects of Humic Acid and Iron Oxyhydroxide Grain-
787   Coating on Biochar Nanoparticle Transport in Saturated Sand. *Environ. Sci. Technol.* **2013,** *47* (10), 5154-
788   5161.
789   18.   Wang, D.; Zhang, W.; Hao, X.; Zhou, D. Transport of Biochar Particles in Saturated Granular
790   Media: Effects of Pyrolysis Temperature and Particle Size. *Environ. Sci. Technol.* **2013,** *47* (2), 821-828.
791   19.   Kasel, D.; Bradford, S. A.; Šimůnek, J.; Heggen, M.; Vereecken, H.; Klumpp, E. Transport and
792   retention of multi-walled carbon nanotubes in saturated porous media: Effects of input concentration
793   and grain size. *Water Research* **2013,** *47* (2), 933-944.
794   20.   Wang, Y.; Becker, M. D.; Colvin, V. L.; Abriola, L. M.; Pennell, K. D. Influence of Residual Polymer
795   on Nanoparticle Deposition in Porous Media. *Environ. Sci. Technol.* **2014,** *48* (18), 10664-10671.
796   21.   Li, Y.; Wang, Y.; Pennell, K. D.; Abriola, L. M. Investigation of the Transport and Deposition of
797   Fullerene (C60) Nanoparticles in Quartz Sands under Varying Flow Conditions. *Environ. Sci. Technol.*
798   **2008,** *42* (19), 7174-7180.
799   22.   Solovitch, N.; Labille, J.; Rose, J.; Chaurand, P.; Borschneck, D.; Wiesner, M. R.; Bottero, J.-Y.
800   Concurrent Aggregation and Deposition of TiO2 Nanoparticles in a Sandy Porous Media. *Environ. Sci.*
801   *Technol.* **2010,** *44* (13), 4897-4902.
802   23.   Chen, G.; Liu, X.; Su, C. Transport and Retention of TiO2 Rutile Nanoparticles in Saturated Porous
803   Media under Low-Ionic-Strength Conditions: Measurements and Mechanisms. *Langmuir* **2011,** *27* (9),
804   5393-5402.
805   24.   Krol, M. M.; Oleniuk, A. J.; Kocur, C. M.; Sleep, B. E.; Bennett, P.; Xiong, Z.; O'Carroll, D. M. A
806   Field-Validated Model for In Situ Transport of Polymer-Stabilized nZVI and Implications for Subsurface
807   Injection. *Environ. Sci. Technol.* **2013,** *47* (13), 7332-7340.

808   25.   Mattison, N. T.; O'Carroll, D. M.; Kerry Rowe, R.; Petersen, E. J. Impact of Porous Media Grain
809   Size on the Transport of Multi-walled Carbon Nanotubes. *Environ. Sci. Technol.* **2011,** *45* (22), 9765-
810   9775.
811   26.   Liu, X. Y.; O'Carroll, D. M.; Petersen, E. J.; Huang, Q. G.; Anderson, C. L. Mobility of Multiwalled
812   Carbon Nanotubes in Porous Media. *Environ. Sci. Technol.* **2009,** *43* (21), 8153-8158.
813   27.   Taghavy, A.; Mittelman, A.; Wang, Y.; Pennell, K. D.; Abriola, L. M. Mathematical Modeling of the
814   Transport and Dissolution of Citrate-Stabilized Silver Nanoparticles in Porous Media. *Environ. Sci.*
815   *Technol.* **2013,** *47* (15), 8499-8507.
816   28.   Lecoanet, H. F.; Bottero, J.-Y.; Wiesner, M. R. Laboratory Assessment of the Mobility of
817   Nanomaterials in Porous Media. *Environ. Sci. Technol.* **2004,** *38* (19), 5164-5169.
818   29.   Tong, M.; Johnson, W. P. Excess Colloid Retention in Porous Media as a Function of Colloid Size,
819   Fluid Velocity, and Grain Angularity. *Environ. Sci. Technol.* **2006,** *40* (24), 7725-7731.
820   30.   Jaisi, D. P.; Elimelech, M. Single-Walled Carbon Nanotubes Exhibit Limited Transport in Soil
821   Columns. *Environ. Sci. Technol.* **2009,** *43* (24), 9161-9166.
822   31.   El Badawy, A. M.; Aly Hassan, A.; Scheckel, K. G.; Suidan, M. T.; Tolaymat, T. M. Key Factors
823   Controlling the Transport of Silver Nanoparticles in Porous Media. *Environ. Sci. Technol.* **2013**.
824   32.   Lin, S. H.; Cheng, Y. W.; Bobcombe, Y.; Jones, K. L.; Liu, J.; Wiesner, M. R. Deposition of Silver
825   Nanoparticles in Geochemically Heterogeneous Porous Media: Predicting Affinity from Surface
826   Composition Analysis. *Environ. Sci. Technol.* **2011,** *45* (12), 5209-5215.
827   33.   Ryan, J. N.; Harvey, R. W.; Metge, D.; Elimelech, M.; Navigato, T.; Pieper, A. P. Field and
828   Laboratory Investigations of Inactivation of Viruses (PRD1 and MS2) Attached to Iron Oxide-Coated
829   Quartz Sand. *Environ. Sci. Technol.* **2002,** *36* (11), 2403-2413.
830   34.   Phenrat, T.; Kim, H. J.; Fagerlund, F.; Illangasekare, T.; Lowry, G. V. Empirical correlations to
831   estimate agglomerate size and deposition during injection of a polyelectrolyte-modified Fe-0
832   nanoparticle at high particle concentration in saturated sand. *Journal of Contaminant Hydrology* **2010,**
833   *118* (3-4), 152-164.
834   35.   Phenrat, T.; Song, J. E.; Cisneros, C. M.; Schoenfelder, D. P.; Tilton, R. D.; Lowry, G. V. Estimating
835   Attachment of Nano- and Submicrometer-particles Coated with Organic Macromolecules in Porous
836   Media: Development of an Empirical Model. *Environ. Sci. Technol.* **2010,** *44* (12), 4531-4538.
837   36.   Yao, K.-M.; Habibian, M. T.; O'Melia, C. R. Water and waste water filtration. Concepts and
838   applications. *Environ. Sci. Technol.* **1971,** *5* (11), 1105-1112.
839   37.   Rajagopalan, R.; Tien, C. TRAJECTORY ANALYSIS OF DEEP-BED FILTRATION WITH SPHERE-IN-CELL
840   POROUS-MEDIA MODEL. *Aiche J.* **1976,** *22* (3), 523-533.
841   38.   Nelson, K. E.; Ginn, T. R. New collector efficiency equation for colloid filtration in both natural
842   and engineered flow conditions. *Water Resour. Res.* **2011,** *47*, 17.
843   39.   Cushing, R. S.; Lawler, D. F. Depth Filtration: Fundamental Investigation through Three-
844   Dimensional Trajectory Analysis. *Environ. Sci. Technol.* **1998,** *32* (23), 3793-3801.
845   40.   Tufenkji, N.; Elimelech, M. Correlation equation for predicting single-collector efficiency in
846   physicochemical filtration in saturated porous media. *Environ. Sci. Technol.* **2004,** *38* (2), 529-536.
847   41.   Ma, H.; Pedel, J.; Fife, P.; Johnson, W. P. Hemispheres-in-Cell Geometry to Predict Colloid
848   Deposition in Porous Media. *Environ. Sci. Technol.* **2009,** *43* (22), 8573-8579.
849   42.   Messina, F.; Marchisio, D. L.; Sethi, R. An extended and total flux normalized correlation
850   equation for predicting single-collector efficiency. *Journal of Colloid and Interface Science* **2015,** *446*,
851   185-193.
852   43.   Ma, H.; Hradisky, M.; Johnson, W. P. Extending Applicability of Correlation Equations to Predict
853   Colloidal Retention in Porous Media at Low Fluid Velocity. *Environ. Sci. Technol.* **2013,** *47* (5), 2272-2278.

854   44.   Pazmino, E. F.; Trauscht, J.; Dame, B.; Johnson, W. P. Power Law Size-Distributed Heterogeneity
855   Explains Colloid Retention on Soda Lime Glass in the Presence of Energy Barriers. *Langmuir* **2014,** *30*
856   (19), 5412-5421.
857   45.   Boccardo, G.; Marchisio, D. L.; Sethi, R. Microscale simulation of particle deposition in porous
858   media. *Journal of Colloid and Interface Science* **2014,** *417* (0), 227-237.
859   46.   Long, W.; Hilpert, M. A Correlation for the Collector Efficiency of Brownian Particles in Clean-Bed
860   Filtration in Sphere Packings by a Lattice-Boltzmann Method. *Environ. Sci. Technol.* **2009,** *43* (12), 4419-
861   4424.
862   47.   Happel, J. VISCOUS FLOW IN MULTIPARTICLE SYSTEMS - SLOW MOTION OF FLUIDS RELATIVE TO
863   BEDS OF SPHERICAL PARTICLES. *Aiche J.* **1958,** *4* (2), 197-201.
864   48.   Nelson, K. E.; Ginn, T. R. Colloid Filtration Theory and the Happel Sphere-in-Cell Model Revisited
865   with Direct Numerical Simulation of Colloids. *Langmuir* **2005,** *21* (6), 2173-2184.
866   49.   Molnar, I. L.; Willson, C. S.; O'Carroll, D. M.; Rivers, M. L.; Gerhard, J. I. Method for Obtaining
867   Silver Nanoparticle Concentrations within a Porous Medium via Synchrotron X-ray Computed
868   Microtomography. *Environ. Sci. Technol.* **2014,** *48* (2), 1114-1122.
869   50.   Cardenas, M. B. Three-dimensional vortices in single pores and their effects on transport.
870   *Geophysical Research Letters* **2008,** *35* (18), L18402.
871   51.   Torkzaban, S.; Tazehkand, S. S.; Walker, S. L.; Bradford, S. A. Transport and fate of bacteria in
872   porous media: Coupled effects of chemical conditions and pore space geometry. *Water Resour. Res.*
873   **2008,** *44* (4).
874   52.   Li, Z.; Zhang, D. X.; Li, X. Tracking colloid transport in real pore structures: Comparisons with
875   correlation equations and experimental observations. *Water Resour. Res.* **2012,** *48* (5), W05533.
876   53.   Kocur, C. M.; Chowdhury, A. I.; Sakulchaicharoen, N.; Boparai, H. K.; Weber, K. P.; Sharma, P.;
877   Krol, M. M.; Austrins, L.; Peace, C.; Sleep, B. E.; O'Carroll, D. M. Characterization of nZVI Mobility in a
878   Field Scale Test. *Environ. Sci. Technol.* **2014,** *48* (5), 2862-2869.
879   54.   Sakulchaicharoen, N.; O'Carroll, D. M.; Herrera, J. E. Enhanced stability and dechlorination
880   activity of pre-synthesis stabilized nanoscale FePd particles. *Journal of Contaminant Hydrology* **2010,** *118*
881   (3–4), 117-127.
882   55.   Oh, W.; Lindquist, W. B. Image thresholding by indicator kriging. *Ieee Transactions on Pattern
883   Analysis and Machine Intelligence* **1999,** *21* (7), 590-602.
884   56.   Bhattad, P.; Willson, C. S.; Thompson, K. E. In *Segmentation of low-contrast three-phase X-Ray
885   Computed Tomography images of porous media*, Proceedings of the GeoX 2010: 3rd International
886   Workshop on X-ray CT for Geomaterials, New Orleans, LA, 2010; Alshibli, K.; Reed, A. H., Eds., pp 254-
887   261.
888   57.   Thompson, K. E.; Willson, C. S.; Zhang, W. L. Quantitative computer reconstruction of particulate
889   materials from microtomography images. *Powder Technology* **2006,** *163* (3), 169-182.
890   58.   Thompson, K. E.; Willson, C. S.; White, C. D.; Nyman, S. L.; Bhattacharya, J. P.; Reed, A. H.
891   Application of a new grain-based reconstruction algorithm to microtomography images for quantitative
892   characterization and flow modeling. *Spe Journal* **2008,** *13* (2), 164-176.
893   59.   Lane, N. M. Numerical studies of flow in porous media using an unstructured approach. Doctor
894   of Philosophy, Louisiana State University, December 2011.
895   60.   Takbiri Borujeni, A.; Lane, N. M.; Thompson, K.; Tyagi, M. Effects of image resolution and
896   numerical resolution on computed permeability of consolidated packing using LB and FEM pore-scale
897   simulations. *Computers & Fluids* **2013,** *88* (0), 753-763.
898   61.   Sanematsu, P.; Shen, Y.; Thompson, K.; Yu, T.; Wang, Y.; Chang, D.-L.; Alramahi, B.; Takbiri-
899   Borujeni, A.; Tyagi, M.; Willson, C. Title: Image-based Stokes flow modeling in bulk proppant packs and
900   propped fractures under high loading stresses. *Journal of Petroleum Science and Engineering* **2015**.

901   62.   O'Carroll, D. M.; Bradford, S. A.; Abriola, L. M. Infiltration of PCE in a system containing spatial
902   wettability variations. *Journal of Contaminant Hydrology* **2004,** *73* (1-4), 39-63.
903   63.   Elimelech, M. PARTICLE DEPOSITION ON IDEAL COLLECTORS FROM DILUTE FLOWING
904   SUSPENSIONS - MATHEMATICAL FORMULATION, NUMERICAL-SOLUTION, AND SIMULATIONS. *Sep.*
905   *Technol.* **1994,** *4* (4), 186-212.
906   64.   Willson, C.; Lu, N.; Likos, W. Quantification of Grain, Pore, and Fluid Microstructure of
907   Unsaturated Sand from X-Ray Computed Tomography Images. *Geotechnical Testing Journal* **2012,** *35* (6),
908   1-13.
909   65.   Pazmino, E. F.; Ma, H. L.; Johnson, W. P. Applicability of Colloid Filtration Theory in Size-
910   Distributed, Reduced Porosity, Granular Media in the Absence of Energy Barriers. *Environ. Sci. Technol.*
911   **2011,** *45* (24), 10401-10407.
912   66.   Ma, H.; Johnson, W. P. Colloid Retention in Porous Media of Various Porosities: Predictions by
913   the Hemispheres-in-Cell Model. *Langmuir* **2009,** *26* (3), 1680-1687.
914   67.   Seetha, N.; Majid Hassanizadeh, S.; Mohan Kumar, M. S.; Raoof, A. Correlation equations for
915   average deposition rate coefficients of nanoparticles in a cylindrical pore. *Water Resour. Res.* **2015**, n/a-
916   n/a.
917   68.   Long, W.; Huang, H.; Serlemitsos, J.; Liu, E.; Reed, A. H.; Hilpert, M. Pore-scale study of the
918   collector efficiency of nanoparticles in packings of nonspherical collectors. *Colloids and Surfaces A:*
919   *Physicochemical and Engineering Aspects* **2010,** *358* (1–3), 163-171.
920   69.   *Environmental and human health impacts of nanotechnology [electronic resource] / edited by*
921   *Jamie R. Lead, Emma Smith*.
922   70.   Ma, H.; Johnson, W. P. Colloid Retention in Porous Media of Various Porosities: Predictions by
923   the Hemispheres-in-Cell Model. *Langmuir* **2010,** *26* (3), 1680-1687.
924   71.   Ma, H.; Pazmino, E.; Johnson, W. P. Surface Heterogeneity on Hemispheres-in-Cell Model Yields
925   All Experimentally-Observed Non-Straining Colloid Retention Mechanisms in Porous Media in the
926   Presence of Energy Barriers. *Langmuir* **2011,** *27* (24), 14982-14994.
927   72.   Kocur, C. M.; O'Carroll, D. M.; Sleep, B. E. Impact of nZVI stability on mobility in porous media.
928   *Journal of Contaminant Hydrology* **2013,** *145* (0), 17-25.
929   73.   Bai, R.; Tien, C. Particle Deposition under Unfavorable Surface Interactions. *Journal of Colloid*
930   *and Interface Science* **1999,** *218* (2), 488-499.
931   74.   Elimelech, M.; Omelia, C. R. EFFECT OF PARTICLE-SIZE ON COLLISION EFFICIENCY IN THE
932   DEPOSITION OF BROWNIAN PARTICLES WITH ELECTROSTATIC ENERGY BARRIERS. *Langmuir* **1990,** *6* (6),
933   1153-1163.
934   75.   Tiraferri, A.; Sethi, R. Enhanced transport of zerovalent iron nanoparticles in saturated porous
935   media by guar gum. *J. Nanopart. Res.* **2009,** *11* (3), 635-645.

936